



UNIVERSITY OF LEEDS

This is a repository copy of *Classification of breast lesions in ultrasonography using sparse logistic regression and morphology-based texture features*.

White Rose Research Online URL for this paper:  
<http://eprints.whiterose.ac.uk/135011/>

Version: Accepted Version

---

**Article:**

Nemat, H, Fehri, H, Ahmadinejad, N et al. (2 more authors) (2018) Classification of breast lesions in ultrasonography using sparse logistic regression and morphology-based texture features. *Medical Physics*, 45 (9). pp. 4112-4124. ISSN 0094-2405

<https://doi.org/10.1002/mp.13082>

---

© 2018 American Association of Physicists in Medicine. This is the peer reviewed version of the following article: Nemat, H. , Fehri, H. , Ahmadinejad, N. , Frangi, A. F. and Gooya, A. (2018), Classification of breast lesions in ultrasonography using sparse logistic regression and morphology-based texture features. *Med. Phys.*, 45: 4112-4124, which has been published in final form at <https://doi.org/10.1002/mp.13082>. This article may be used for non-commercial purposes in accordance with Wiley Terms and Conditions for Self-Archiving. Uploaded in accordance with the publisher's self-archiving policy.

**Reuse**

Items deposited in White Rose Research Online are protected by copyright, with all rights reserved unless indicated otherwise. They may be downloaded and/or printed for private study, or other acts as permitted by national copyright laws. The publisher or other rights holders may allow further reproduction and re-use of the full text version. This is indicated by the licence information on the White Rose Research Online record for the item.

**Takedown**

If you consider content in White Rose Research Online to be in breach of UK law, please notify us by emailing [eprints@whiterose.ac.uk](mailto:eprints@whiterose.ac.uk) including the URL of the record and the reason for the withdrawal request.



[eprints@whiterose.ac.uk](mailto:eprints@whiterose.ac.uk)  
<https://eprints.whiterose.ac.uk/>

# Classification of Breast Lesions in Ultrasonography Using Sparse Logistic Regression and Morphology-based Texture Features

Hoda Nemat<sup>1</sup>, Hamid Fehri<sup>1</sup>, Nasrin Ahmadinejad<sup>2</sup>, Alejandro F. Frangi<sup>1</sup>, and Ali Gooya<sup>1</sup>

<sup>1</sup>Center for Computational Imaging Simulation Technologies in Biomedicine (CISTIB), Department of Electronic and Electrical Engineering, University of Sheffield, Sheffield, S1 3JD, United Kingdom

<sup>2</sup>Department of Radiology, Faculty of Medicine, Tehran University of Medical Sciences, Tehran, 1416753955, Iran

Author for correspondence: Ali Gooya

Email: [a.gooya@sheffield.ac.uk](mailto:a.gooya@sheffield.ac.uk)

Phone: +44 114 222 5397

## I. Abstract

Purpose:

This work proposes a new reliable Computer Aided Diagnostic (CAD) system for the diagnosis of breast cancer from Breast Ultrasound (BUS) images. The system can be useful to reduce the number of biopsies and pathological tests, which are invasive, costly, and often unnecessary.

Methods:

The proposed CAD system classifies breast tumors into benign and malignant classes using morphological and textural features extracted from Breast Ultrasound (BUS) images. The images are first pre-processed to enhance the edges and filter the speckles. The tumor is then segmented semi-automatically using the watershed method. Having the tumor contour, a set of 855 features including: 21 shape-based, 810 contour-based, and 24 textural features are extracted from each tumor. Then, a Bayesian Automatic Relevance Detection (ARD) mechanism is used for computing the discrimination power of different features and dimensionality reduction. Finally, a logistic regression classifier computed the posterior probabilities of malignant versus benign tumors using the reduced set of features.

Results:

A dataset of 104 BUS images of breast tumors, including 72 benign and 32 malignant tumors, was used for evaluation using 8-fold cross-validation. The algorithm outperformed six state-of-the-art methods for BUS image classification with large margins by achieving 97.12% accuracy, 93.75% sensitivity, and 98.61% specificity rates.

Conclusions:

Using ARD, the proposed CAD system selects 5 new features for breast tumor classification and outperforms state-of-the-art, making a reliable and complementary tool to help clinicians diagnose breast cancer.

Keywords: Classification, computer-aided diagnosis, logistic regression, segmentation, ultrasound images.

## II. Introduction

Breast cancer is the second fatal disease in women<sup>1</sup>, and its early diagnosis is important for longer patient survival<sup>2,3</sup>. Breast cancer diagnostic techniques include clinical examination, medical imaging, and biopsy. Among the imaging methods, ultrasonography is usually utilized due to its advantages such as being real-time and cost-effective, not using ionizing radiation, and showing high sensitivity in dense tissues. Despite its advantages, the noisy nature of ultrasound images and the overlapping features of benign and malignant masses lead to difficulties in diagnosis. Therefore, usually, performing a biopsy is the most accurate diagnostic method. However, since only 10 to 30 percent of the biopsies are malignant, reducing unnecessary biopsies is highly desirable<sup>2-8</sup>. Computer-aided diagnosis systems are a candidate for this purpose.

Using CAD systems for breast cancer has five stages: pre-processing, segmentation, feature extraction, feature selection, and classification. In Breast Ultrasound (BUS) image pre-processing, the contrast between the lesion region and the background should be increased (image enhancement). Some specific pre-processing methods are capable of reducing speckle without destroying the important features of BUS images (speckle reduction)<sup>1,3,9-11</sup>. Lesion region is separated from the background and other tissue structures through segmentation<sup>1,2</sup>. In the literature, tumor segmentation has been done automatically<sup>6,12,13</sup>, semi-automatically<sup>11,14,15</sup> or manually by the radiologist<sup>16,17</sup>. Two main types of features are extracted for BUS image analysis; morphological and textural features. Morphological features represent local characteristics of the

tumor lesion and are used to quantify malignancy using shape, contour or boundary characteristics<sup>1-3,5,11,18</sup>. Textural features explain internal echo patterns and the composition of the encompassing tissues and are selected from the original or pre-processed images<sup>1-3,5,6,11</sup>. For feature extraction, Genetic algorithm<sup>19</sup>, mutual information<sup>11</sup>, statistical tests<sup>20</sup>, Relief and FOCUS techniques<sup>21</sup> have been utilized for breast ultrasound images. Breast tumor classification in ultrasound images has been done using linear classifiers (linear discriminant analysis, logistic regression), artificial neural networks, Bayesian neural networks, decision tree, support vector machine and template matching<sup>1-3</sup>. Table (1) summarizes some of the characteristics of the techniques used in the literature in a chronological order.

Table (1): Survey of recent CAD systems

Reference	BUS dataset	Segmentation	Best feature set	Feature selection	Classifier
Yousef-2016 <sup>18</sup>	99 53 B, 46 M	Manual	6 Morph	Wrapper method	NN, KNN, NC, LDA
Abdelwahed-2015 <sup>22</sup>	80 44 B, 36 M	Semi-automatic	9 Text	NA	KNN, SVM, CART
Gomez_2015 <sup>11</sup>	641 413 B, 228 M	Semi-automatic	26 Morph & 1465 Text	Mutual information & Statistical tests	LDA
Lokesh-2014 <sup>23</sup>	50 38 B, 12 M	Semi-automatic	8 Text	NA	SVM
Moon-2013 <sup>24</sup>	69 48 B, 21 M	Semi-automatic	5 Morph & 1 Text	Student's t test	LR
Alvarenga-2012 <sup>25</sup>	246 69 B, 177 M	Semi-automatic	2 Morph & 3 Text	Statistical approaches	LDA
Wu-2012 <sup>19</sup>	210 120 B, 90 M	Automatic	2 Morph & 3 Text	Genetic Algorithms	SVM
Zakeri-2012 <sup>26</sup>	80 47 B, 33 M	Automatic	4 Morph & 2 Text	NA	SVM
Su-2011 <sup>6</sup>	132 67 B, 65 M	Automatic	5 Morph & 3 Text	Principle Component Analysis	NN
Behnam-2010 <sup>27</sup>	81 47 B, 34 M	Automatic	7 Morph	NA	NN
Alvarenga-2010 <sup>28</sup>	246 69 B, 177 M	Semi-automatic	3 Morph	Statistical approaches	LDA
Wu-2008 <sup>29</sup>	210 120 B, 90 M	Automatic	1 Morph & 8 Text	Forward feature selection	SVM
Shen-2007 <sup>20</sup>	265 180 B, 85 M	Manual	4 Morph & 4 Text	Student's t test	LR
Chang-2005 <sup>12</sup>	210 120 B, 90 M	Automatic	6 Morph	NA	SVM
Sehgal-2004 <sup>17</sup>	58 38 B, 20 M	Manual	3 Morph	NA	LR
Chen-2003 <sup>16</sup>	271 131 B, 140 M	Manual	6 Morph	Statistical approaches	NN
Horsch-2002 <sup>30</sup>	400 306 B, 94 M	Automatic	2 Morph & 1 Text	NA	LDA

B: Benign; M: Malignant; Morph: Morphology; Text: Texture; NA: Not Applied; NN: Neural Network; KNN: K-Nearest Neighbor; NC: Nearest Centroid; SVM: Support Vector Machine; CART: Classification & Regression Trees; LR: Logistic Regression; LDA: Linear Discriminant Analysis.

Morphological and textural features and their combination have been compared based on their discrimination power in classification, without a clear conclusion. For instance, Alvarenga et al.<sup>25</sup> studied 7 morphological and 20 textural features and concluded that the combination can be useful. Using 26 morphological and 1465 textural features, Gomez et al.<sup>11</sup> concluded that using morphological features alone results in a better classification. A wide range of morphological<sup>12,14,17,26,27,31,32</sup>, textural features<sup>5,33-35</sup> or their combinations<sup>6,19,26,36</sup> have been used. Despite the broad range of existing methods, each implementing a distinctive form of feature sets, an amalgamation of information of these feature groups has not been studied. In this study, we elaborate different morphological/textural features and their derivations to evaluate their differentiation ability in a single framework. We also introduce a new combined category of features using information of shape and gray-level values of the boundary. Finally, we apply an automatic approach for finding an effective feature set that successfully classifies tumors into malignant and benign classes. Our method identifies the most clinically relevant features for diagnosis, which is in contrary to methods that use convolutional networks<sup>37-39</sup> to learn highly discriminative features that can be extracted from the entire image area and can be hard to interpret. These methods require large data sets to avoid overfitting.

We propose a reliable CAD system to identify breast tumor types. After a pre-processing and semi-automatic segmentation, the ROI is determined automatically. A pool of features containing both morphological and textural features is calculated. Automatic Relevance Determination (ARD)<sup>40</sup> is used for feature selection that removes subjective interpretations and provides a sound data-driven approach to study the effect of feature combination. Finally, we introduce a new set of textural features based on morphology with a high discrimination power in tumor classification. Using the new set of features, the tumors are diagnosed in each image in a dataset of 104 breast tumor BUS images. We follow the naming provided by a subcommittee of the Japan Association of Breast and Thyroid Sonology<sup>41</sup>. As shown in Fig. 1, the area including contour, margin, and the periphery of the tumor is called the boundary zone, where, the contour is the plane between the tumor and the tissue around it, the margin is the peripheral part of the tumor adjacent to the contour and periphery is the surrounding area of the tumor.

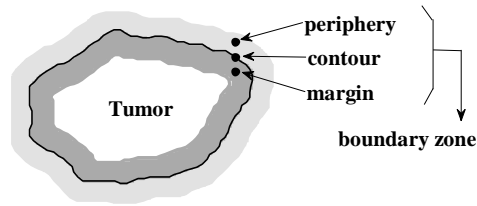


Fig. 1. The margin, contour, periphery, and the boundary zones.

The rest of paper is organized as follows. Sections 3 and 4 present the details of the dataset and the proposed method. In Section 4, experimental results are explained. The discussion and conclusion are drawn in Sections 5 and 6, respectively.

### III. Materials and methods

The dataset used in the study includes 104 BUS images from breast tumors with 72 benign and 32 malignant tumors, which belonged to three grades (I, II, III) and were divided into these invasive types: ductal, mucinous, and tubular, lobular carcinomas. Most cases were invasive ductal carcinoma in grade II. To create the Confusion matrix, types of tumors in images are determined based on pathological examinations or following a two-year examination schedule. The images were taken from patients that referred to The Radiology Department of Imam Khomeini Hospital, Tehran, Iran. All subjects gave their written informed consent to participate in the following studies that were acquired using various sonography machines across different periods:

- 19 February 2006 to 22 August 2008, Antares (Siemens, Germany), VFX 13–5 (Multi-D) linear array transducer, DICOM format, 56 ultrasonography images (34 benign and 22 malignant),
- 28 May 2013 to 15 November 2013, Zonare (General Electric, US), SP6–12 linear array transducer, tiff format, 35 ultrasonography images (27 benign and 8 malignant), and
- 23 June 2015 to 9 November 2015, Sonix OP (Ultrasonic, Germany), 5–14 MHz linear array transducer, jpg format, 13 ultrasonography images (11 benign and 2 malignant).

The rest of this section explains the proposed CAD system consisting of pre-processing, segmentation, and extraction of the region of interest, feature extraction and classification of the breast US images.

#### 1. Pre-processing

Speckles resulting from the interaction of ultrasonic waves with tissue degrade the quality of Ultrasound (US) images. Pre-processing US images should enhance edge information and suppress speckle efficiently whilst preserving lesion boundaries and structure details. Hence, it includes two steps of contrast enhancement and speckle filtering. We used Contrast Limited Adaptive Histogram Equalization (CLAHE) technique<sup>42</sup> for contrast enhancement and removed the speckles with anisotropic diffusion filtering<sup>9</sup>. The parameters used for CLAHE technique and speckle filtering were the default MATLAB values and those used in Gomez et al.<sup>9</sup>, respectively.

#### 2. Segmentation

Tumor contours can be delineated manually or automatically. However, the details of the contour may be eliminated in manual delineation, particularly in malignant tumors. This information is important when morphological features are extracted. Existing computerized segmentation algorithms cannot always provide the required accuracy, especially in complex lesion boundaries<sup>9,13,43</sup>. To address these limitations, we propose a combination of manual and computerized approaches to improve segmentation.

We first use watershed to extract the contour of each tumor by using MATLAB software. Initially, three contours are generated corresponding to three values of the hyper-parameter of constraint Gaussian function, which scales the contour by 2, 2.2 and  $2\pi$  and generates the most visually accurate contours using the method presented in Gomez et al.<sup>9</sup>. Next, an expert radiologist verifies the most accurate segmentation from the set of generated contours for each tumor and manually corrects them with Didger5 software<sup>44</sup> (see Fig. 2).

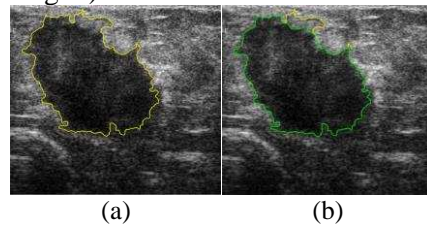


Fig. 2. (a) A BUS image of a malignant tumor and its most appropriate computerized contour (yellow line), (b) The edited tumor contours with Didger5 software (green), showing elimination of parts wrongly considered as a tumor.

### 3. ROI extraction

In the literature, the area around the tumor is removed manually before pre-processing to reduce the computational burden. However, we propose to remove these areas after determination of the tumor contour. Doing this has two benefits: first, the information in the surrounding area can help in drawing the tumor contour. Second, all tumor ROIs are extracted automatically and are therefore more consistent.

To eliminate non-tumor associated areas in the image, an external tumor contour is specified using a morphological dilation operator by a disk structuring element with 30 pixels' radius (Fig. 3b). Then a circumscribed rectangle (the smallest rectangle containing the external contour) is obtained (Fig. 3c), and the image is cropped according to the rectangle.

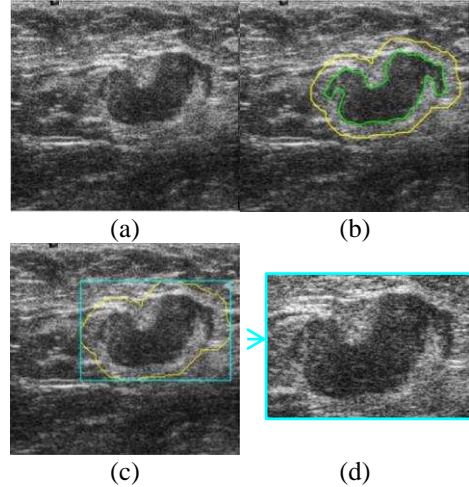


Fig. 3. Extraction of ROI; a BUS image containing a tumor (a), the contour of the tumor (green) and the associated external contour (yellow) (b), the circumscribed rectangle (c), and the extracted ROI from the primary image (d).

### 4. Feature extraction

Benign tumors have more regular shapes compared to malignant ones. Most of the benign tumors have round or ellipsoid shapes with smooth and well-defined contours and homogeneous internal echoes. Malignant tumors have heterogeneous internal echoes, branch patterns, irregular and blurred boundaries, and ill-defined contours. To use the mentioned characteristics for classification of tumors, usually shapes, tumor surroundings, and internal echo patterns are modeled, which are expressed as morphological and textural features<sup>2,3,7,8,12,14,45</sup>. In this section, we investigate these two categories of features and extend contour-based features by introducing signatures. We also apply a novel boundary extraction method and use morphology-based textural features to discriminate malignant breast tumors. Morphology-based textural features, called textural features in this paper for simplicity, employ a combination of morphology and texture to extract comprehensive information from the tumor boundary. Fig. 4 depicts the categorization of features used for classification in this study.

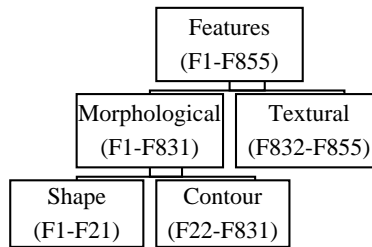


Fig. 4. Categorization of the investigated and presented features.

In the sequel, we discuss details of the implemented features.

#### a) Morphological features

By morphological features in this paper, we refer to two categories: shape-based features extracted from 2D masks, and contour-based features extracted from one dimensional signatures. For extraction of shape-based features, a binary image of the tumor shape in two dimensions is used (Fig. 5b). For contour-based features, we use the tumor contour (Fig. 5c) and represent it as a one-dimensional signal.

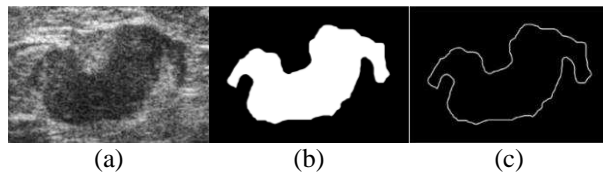


Fig. 5. The BUS image of a malignant tumor (a), the binary image of tumor shape (b), and the contour of the tumor (c).

(1) Shape Features

Twenty-one shape-based features that are most frequently used for breast tumor diagnosis are implemented (for details see Appendix A).

(2) Contour Features

Contour-based features are derived from a one-dimensional representation of the tumor contour, called a signature. Signatures based on radial distance and complex coordinates<sup>46-54</sup> are already implemented in the literature for tumor type classification<sup>1,2,9,11,36,55-58</sup>. We extend the use of signatures by generating seven new transformations describing the contour in different parametric spaces, namely: polar coordinates<sup>53</sup>, farthest point distances<sup>49,53,54</sup>, farthest point angle<sup>54</sup>, angular function<sup>51-53,59</sup>, angular radial coordinate<sup>53</sup>, contour curvature<sup>47,49,52,54,59-61</sup>, and triangle area function<sup>49,51-53</sup>. We use nine signatures in total. Spatial and frequency information (i.e. Fourier descriptors and their statistics) is then extracted from these signatures (see Fig. 6). The explanation of these signatures is provided in Appendix B.

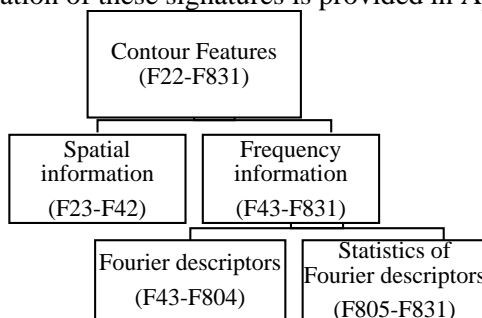


Fig. 6. Categorization of contour features.

To extract spatial information from signatures, the values of mean, standard deviation, smoothness index, roughness index and zero crossings<sup>14,55</sup> are calculated for four real signatures consisting of radial distance, farthest point distance, farthest point angle, and triangle area function. For radial distance signature, area ratio<sup>11,14</sup> is also calculated. In this step, 21 spatial information based contour features are extracted.

Next, to study the frequency information of the contour, Discrete Fourier Transform (DFT) is used. For this purpose, the number of points representing each signature, i.e. signature vector size, is normalized and its DFT coefficients are used as features. Since for a better performance of DFT, the signature vector size should be a power of two, the contour points have to be sampled before contour signature generation<sup>52</sup>. Let  $N$  denote the signature vector size achieved by 8-connectivity contour tracing procedures<sup>62</sup> and  $L = 2^7 = 128$  denote the number of desirable points after sampling. Also, let  $P$  be the perimeter of the tumor contour. The sampled points are equidistant on the contour, so each two successive points are in  $P/L$  distance from each other (on the contour)<sup>54</sup>.

The coefficients of DFT, called Fourier descriptors, represent the contour in the frequency domain. It can be proven that these Fourier descriptors are invariant to translation, rotation, and scale. Proofs are included in Appendix C.

We collectively computed 762 Fourier descriptors from the nine mentioned signatures. Additionally, for each of them, mean, variance and entropy are computed, leaving 27 statistical features (810 contour-based features in total). Overall, 831 morphological features consisting of 21 shape-based and 810 contour-based features were extracted from each image (see Fig. 4).

b) Textural Features

Features based on the mean grey level differences between inside and outside of the contour have been used for studying tumor boundaries in tumor type classification<sup>1,2,17,31,32,63-67</sup>. However, more comprehensive textural features extracted from the vicinity of the contour can increase the accuracy of tumor classification. For this propose, for each BUS image such as Fig. 7a, we construct a boundary band around the contour of the tumor in Fig. 7b. The band is then unrolled into a new image. The directional and textural information of this image is extracted by a Gabor filter bank. The entropies of filtered images are then calculated and used as the textural features. Steps of calculations involved here are presented in a more detail in the following.

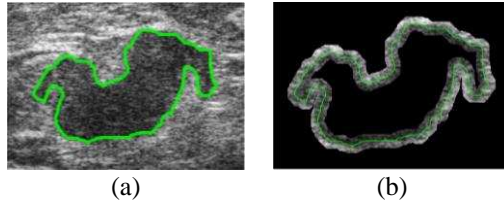


Fig. 7. (a) The BUS image of a malignant tumor and its contour (green), (b) the 20-pixel boundary around the tumor contour. To investigate the tumor boundary area, Sahiner et al.<sup>68-70</sup> introduced the Rubber Band Straightening Transform (RBST) that maps a band of pixels surrounding the mass onto the Cartesian plane (a rectangular region), according to the directions of lines normal to the tumor contour. Their algorithm comprises of three main steps: 1) edge enumeration, 2) normal computation, and 3) computation of RBST pixel values (see Fig. 8).

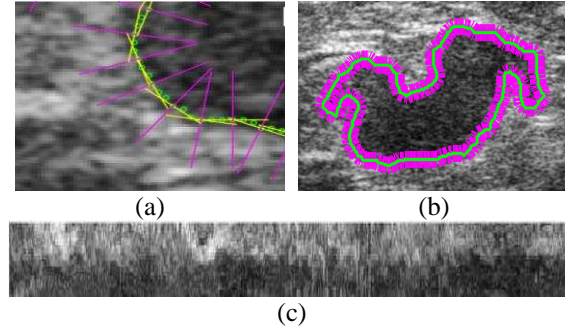


Fig. 8. (a) A close up view of indicator points (green), tangent lines (yellow), and normal lines (magenta) for a part of a malignant tumor contour, (b) all the tumor contour points (green) and the normal lines of contour indicator (magenta), and (c) the resulting RBST image. Despite its proven effectiveness, Sahiner's algorithm fails to provide a uniform sampling of the boundary information for irregular contours. This happens due to the simplistic way of finding normals to the contour, which is prone to error at irregular parts of the boundary like tumor edges (see Fig. 9a).

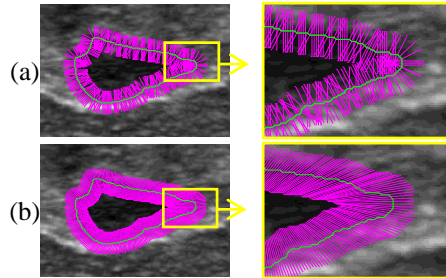
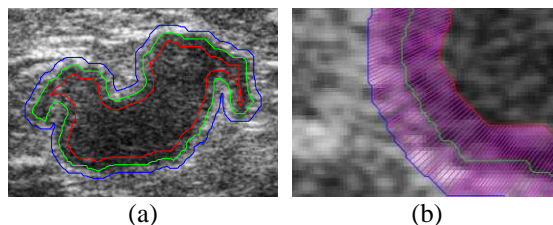


Fig. 9. Contours (green) and the corresponding normals (magenta) are shown for a benign tumor using Sahiner's algorithm (a) and the proposed method (b). The close up views on the right show non-uniform samplings throughout the boundary for Sahiner's algorithm, which are significantly more uniform for the proposed method.

To overcome the limitation of Sahiner's algorithm, we propose Morphology-Based RBST (MBRBST) method that generates the internal and external contours of the tumor (Fig. 9b), using a 10-pixel radius disk structure element for morphological erosion and dilation, respectively (Fig. 10a). After determining the contours, an equal number of points are sampled on each (we used the number of external contour points,  $N$ , as the number of sampling points), which are then correspondingly connected by  $N$  connecting lines (Fig. 10b). Next, the image intensity is sampled at 15 equidistant locations selected on each of the connecting lines (Fig. 10c). Since the selected locations are not exactly at the center of the pixels, they are approximated by centers of pixel they are on, (see Fig. 10d). The sampled intensity levels are sorted from the innermost point (on the internal contour) to the outermost point (on the external contour) in a vector for each connecting line. The resulting  $N$  vectors are then stored in a  $15 \times N$  matrix that represents the corresponding rectangular MBRBST image for the tumor (Fig. 10e).



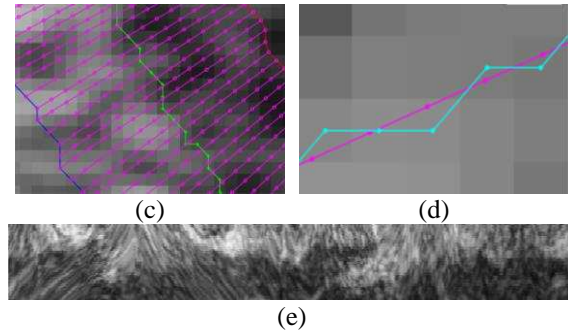


Fig. 10. (a) The tumor contour (green), internal (red) and external (blue) contours 10-pixel away from the main contour, (b) A close up view of the main, internal and external contours and the connecting lines (magenta lines) on a part of the contour, (c) A close up view of the 15 sampled points on the connecting lines, (d) A close up view of an original connecting line, its sampled points (magenta) and their approximated locations (cyan), (e) The resulting MBRBST from the gray level values of the approximated points.

The extracted rubber band consists of shape and texture information that help in classification of tumors. Four sample BUS images, including two malignant and two benign tumors, with parts of their MBRBST images, are shown in Fig. 11. It is seen that MBRBST images well delineate the irregularities of tumors and can, therefore, discriminate their malignancy.

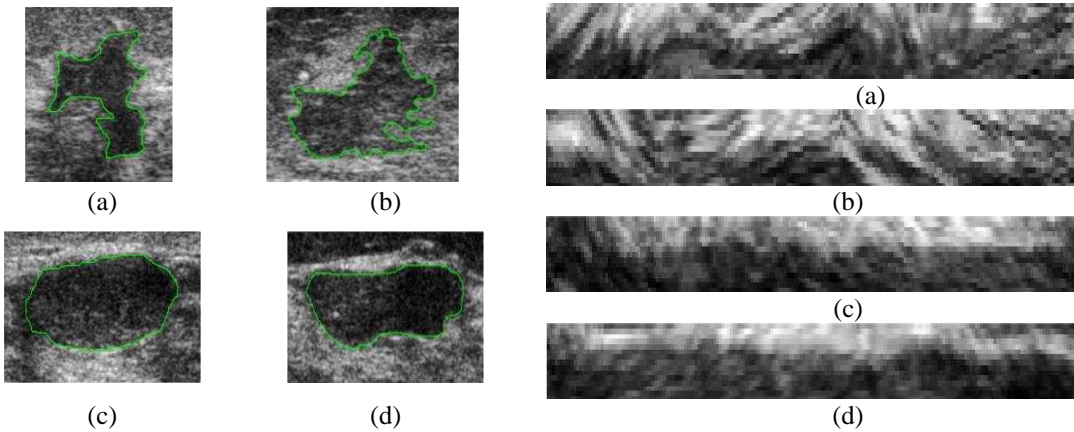


Fig. 11. BUS images of two malignant (a), (b), and two benign (c), (d) tumors and their corresponding MBRBST images.

Gabor filters are used for the detection of directional elements<sup>71-76</sup> in image processing, such as classification and edge detection. In BUS images, these filters are frequently used for preprocessing and speckle reduction<sup>1,2,10,11,77</sup>. In this study, we use 24 Gabor filters with different scales and directions (see Appendix D for details). The Gabor filter bank is applied to each MBRBST image and the entropy of each filtered image is calculated, generating 24 features. With the 831 morphologic features from the previous steps, the total number of 855 features are generated for each image (see Fig. 4).

#### 5. Feature selection and classification

To improve the classification performance and avoid overfitting, features with irrelevant information must be removed. In the literature of breast tumor classification, features are selected prior to classification. Therefore, not all features are used in the classification. In the present study, however, we rely on a joint feature selection and classification mechanism. Specifically, we use Sparse Logistic Regression (SLR)<sup>78</sup>, which is a Bayesian logistic regression method, implementing Automatic Relevance Determination (ARD). Using ARD, the SLR classifier prunes a large set of input features to a sparse set of most discriminative features deriving the classification. The details of the sparse classifier are explained in Appendix E.

### IV. Results

#### 1. Experimental design

We used MATLAB for pre-processing, feature extraction, classification and segmentation, and Didger5 for correcting manual delineations. A dataset of 104 real BUS images was used and overall 855 features were extracted from each image. To evaluate the proposed algorithm, we performed an 8-fold cross validation protocol, where 91 images were used for both feature selection and training, and the remaining 13 images were used for testing and validation. In each fold, leave-one-out experiments were applied on the training set to select the most relevant (discriminant) features. In each experiment, an 855-dimensional weight vector indicating the discrimination powers of all feature is generated by the SLR. This process is repeated until all images in the training set are tested<sup>26</sup>, generating 91 weight vectors. Next, we find the most discriminant

features, whose corresponding weights are non-zero for at least 80% of the leave-one-out experiments. We then use these selected features for classification of the test set. To ensure that the selected features are not coincidental, we altered the order of features randomly for 10 times. We observed that the SLR selected the same features exactly, indicating that they are genuinely relevant to the classification.

A confusion matrix <sup>79</sup> was generated by comparing the results of the proposed classification algorithm with the Confusion matrix. Confusion matrix comprised: True Positives (TP), i.e. number of malignant tumors correctly recognized as malignant; True Negatives (TN), i.e. number of benign tumors that correctly recognized as benign, False Positives (FP), i.e. number of benign tumors that incorrectly recognized as malignant; and False Negatives (FN), i.e. number of malignant tumors that incorrectly recognized as benign.

Accuracy ( $Acc = \frac{TP+TN}{(TP+TN+FP+FN)}$ ), sensitivity ( $Sen = \frac{TP}{(FN+TP)}$ ), specificity ( $Spe = \frac{TN}{(FP+TN)}$ ), positive predictive value ( $PPV = \frac{TP}{(FP+TP)}$ ), negative predictive value ( $NPV = \frac{TN}{(FN+TN)}$ ), and Matthew's correlation coefficient ( $MCC = \frac{(TP \times TN) - (FP \times FN)}{\sqrt{(TP+FP)(TP+FN)(TN+FP)(TN+FN)}}$ ) criteria were used for evaluating the classification performance <sup>14,26,27</sup>.

## 2. Evaluation of the proposed method

Based on the corresponding weights, features F138, F180, F441 (from Fourier descriptors features) and F833, F837 features (from Textural features) were selected in every eight experiments of cross-validation and were therefore used for measuring classification performance. The descriptions of these features are as follows:

- F138: The 98<sup>th</sup> normalized Fourier descriptor ( $\frac{|FD_{98}|}{|FD_1|}$ ) of the complex coordinates signature.
- F180: The 14<sup>th</sup> normalized Fourier descriptor ( $\frac{|FD_{14}|}{|FD_1|}$ ) of the polar coordinates signature.
- F441: The 20<sup>th</sup> normalized Fourier descriptor ( $\frac{|FD_{20}|}{|FD_0|}$ ) of the farthest point angle signature.
- F834: Entropy of the output of the 3<sup>rd</sup> Gabor filter (with scale  $s = 1$  and direction  $d = 3$ ) for MBRBST image.
- F838: Entropy of the output of the 7<sup>th</sup> Gabor filter (with scale  $s = 2$  and direction  $d = 3$ ) for MBRBST image.

The classification performance using the SLR algorithm applied on various categories of features are presented in Table (2). Each row in this table shows a different subset of input features and the classification performance using the features selected by ARD. The feature definitions are given in Appendix F.

Table (2): The performance of the proposed tumor classification method using the selected features from each input subset (mean  $\pm$  standard deviation).

Feature category	Acc (%)	Sen (%)	Spe (%)	PPV (%)	NPV (%)	MCC (%)	Selected Features
All features (F1-F855)	97.12 $\pm$ 3.98	93.75 $\pm$ 11.57	98.61 $\pm$ 3.93	97.50 $\pm$ 7.07	97.50 $\pm$ 4.63	93.58 $\pm$ 8.88	F138, F180, F441, F833, F837
• Morphological (F1-F831)	89.42 $\pm$ 5.72	78.13 $\pm$ 20.86	94.44 $\pm$ 5.94	88.75 $\pm$ 12.17	91.43 $\pm$ 7.75	75.81 $\pm$ 13.81	F10, F12, F760
o Shape-Based (F1-F21)	89.42 $\pm$ 5.72	71.88 $\pm$ 16.02	97.22 $\pm$ 5.14	93.33 $\pm$ 12.85	88.98 $\pm$ 6.08	75.21 $\pm$ 14.71	F12, F15, F16, F19
o Contour-Based (F22-F831)	89.42 $\pm$ 5.72	71.88 $\pm$ 16.02	97.22 $\pm$ 5.14	93.75 $\pm$ 11.57	88.93 $\pm$ 5.70	75.27 $\pm$ 13.46	F33, F62, F166, F513, F800
▪ Spatial information (F22-F42)	81.73 $\pm$ 8.16	62.50 $\pm$ 23.15	90.28 $\pm$ 11.01	81.25 $\pm$ 21.67	85.18 $\pm$ 7.88	58.20 $\pm$ 19.28	F24, F26, F33, F41, F42
▪ Frequency information (F43-F831)	85.58 $\pm$ 6.42	75.00 $\pm$ 18.90	90.28 $\pm$ 7.12	78.75 $\pm$ 13.99	89.72 $\pm$ 7.58	66.70 $\pm$ 16.88	F66, F166, F333, F676, F677, F706, F773
• Fourier descriptors (F43-F804)	89.42 $\pm$ 5.72	81.25 $\pm$ 11.57	93.06 $\pm$ 5.75	85.00 $\pm$ 12.54	91.94 $\pm$ 5.00	75.52 $\pm$ 13.66	F62, F66, F291, F294, F308, F333, F443, F676, F677, F706, F773
• Statistical features of Fourier descriptors (F805-F831)	82.69 $\pm$ 9.86	68.75 $\pm$ 17.68	88.89 $\pm$ 11.88	77.71 $\pm$ 21.25	86.77 $\pm$ 7.10	60.68 $\pm$ 22.04	F806, F808, F809, F814, F817, F831
• Textural (F832-F855)	93.27 $\pm$ 4.93	87.50 $\pm$ 13.36	95.83 $\pm$ 5.75	91.87 $\pm$ 11.32	94.86 $\pm$ 5.51	84.88 $\pm$ 11.47	F832, F833, F834, F836, F838

According to Table (2):

- Combining textural and morphological features and using the whole 855 features gives the best performance.
- The performance of textural features is better than morphological features, when only one category is used.

- Morphological shape-based and contour-based features have similar performances.
- When using only contour-based features, the performance of frequency information is better than spatial information.
- Fourier descriptors result in a more accurate classification compared to statistical features. Also, using a combination of these features results in a lower performance compared to using Fourier descriptors only.

The proposed boundary extraction algorithm (MBRBST) was also compared to Sahiner’s (RBST) and conventional ROI extraction algorithms in terms of their impact on the classification results. For each region extracted by these methods, 24 filtered images were generated by Gabor bank and their entropies were used for classification. The evaluation metrics are defined in the Experimental design subsection. As shown in Table (3), morphology-based textural features created by MBRBST outperform the two other methods. This indicates that the textural and morphological information embedded in the MBRBST features makes them more effective than pure textural features that are derived from conventional ROIs.

Table (3): The performances of features obtained using MBRBST, RBST, and conventional ROI extraction methods.

Filter bank input	Acc (%)	Sen (%)	Spe (%)	PPV (%)	NPV (%)	MCC (%)
MBR	93.27±	87.50±	95.83±	91.87±	94.86±	84.88±
BST	4.93	13.36	5.75	11.32	5.51	11.47
RBST	92.31± 7.12	87.50± 13.36	94.44± 8.40	89.58± 14.60	94.72± 5.66	83.01± 15.67
ROI	84.62± 7.12	65.63± 18.60	93.06± 8.27	83.33± 17.82	85.48± 7.25	63.78± 18.62

We now compare the performance of the proposed algorithm with the six most related algorithms in the literature. Brief summaries of the selected classification methods and the features employed for each of them are included in Table (4).

Table (4): A summary of the specifications and presented results of the implemented methods of the literature.

Reference	BUS dataset	The proposed feature set	Classifier	Acc (%)	Sen (%)	Spe (%)	PPV (%)	NPV (%)
Alvarenga-2012 <sup>25</sup>	246 69 B 177 M	Normalized residual value, Contour roughness, contrast standard deviation, and angular second moment	LDA	85.37	83.62	89.86	95.48	68.13
Alvarenga-2010 <sup>14</sup>	246 69 B 177 M	Normalized residual value, Circularity, and Contour roughness	LDA	83.74	83.05	85.51	93.63	66.29
Behnam-2010 <sup>27</sup>	81 47 B 34 M	Difference area, mean, variance, skewness, kurtosis, and entropy of variation function	NN (MLP)	93.83	91.18	95.74	93.94	93.75
Shen_2007 <sup>20</sup>	256 180 B 85 M	Shape, Orientation, Margin, Lesion boundary, Echo pattern, and Posterior shadowing	LR	91.70	90.59	92.22	84.62	95.40
Chang-2005 <sup>12</sup>	210 120 B 90 M	Form-factor, aspect-ratio, roundness, extent, convexity, and solidity	SVM (RBF)	90.95	88.89	92.50	89.89	91.74
Chen-2003 <sup>16</sup>	271 131 B 140 M	Elliptic-normalized circumference, Elliptic-normalized skeleton, Long axis to short axis ratio, Depth-to-width ratio, Number of substantial protuberances and depressions, and Lobulation index	NN	94.40	97.80	89.90	92.70	96.90

B: Benign; M: Malignant; NN: Neural Network; LDA: Linear Discriminant Analysis; LR: Logistic Regression; SVM: Support Vector Machine.

Since the imaging dataset used for evaluating the selected methods were not publicly available, we evaluated them using our own dataset in this paper. Table (5) represents the results of leave-one-out cross-validations for all methods. We also calculated the area under the receiver operating characteristics (ROC) curve, AUC, as a common measure in the context of CAD systems<sup>80</sup>.

Table (5): Classification results of the proposed algorithm and selected methods applied on our dataset.

Method	Acc (%)	Sen (%)	Spe (%)	PPV (%)	NPV (%)	AUC
Proposed algorithm	97.12	93.75	98.61	97.50	97.50	0.9904
Alvarenga-2012	90.00	83.33	92.86	83.33	92.86	0.9753
Alvarenga-2010	84.62	68.75	91.67	78.57	86.84	0.9042
Behnam-2010	87.50	75.00	93.06	82.76	89.32	0.8983
Shen-2007	83.65	68.75	90.28	75.86	86.67	0.9140
Chang-2005	81.73	68.75	87.50	70.97	86.30	0.8572
Chen-2003	85.00	66.67	92.86	80.00	86.67	0.7942

As seen in Table (5), the proposed method outperforms all the selected methods of the literature. However, we remind that the differences between the performances of the methods from the literature on their original and our dataset can be due to the differences in the levels of difficulty of image databases and/or segmentation methods used.

## V. Discussion

In this study, a dataset of 104 BUS images (72 benign and 32 malignant tumors) was first collected. The images were then segmented through a computerized method followed by a manual delineation carried out by a radiologist. For each tumor, 21 (2D) shape-based, 810 contour-based, and 24 textural features were extracted. Contour-based features are derived from 9 (7 new and 2 existing) signatures that are one dimensional contour representations. The textural features in this work are derived by: unfolding the narrow band that surrounds the tumor boundary, applying the Gabor filter bank to the unfolded image, and computing the entropies. The latter depend on the morphology of the tumor as unfolding more irregular tumor boundaries often results in more directional and complex textures. Hence, the computed entropies are referred to as morphology-based textural features in this work. An SLR classifier, incorporating ARD, was used to automatically select the five most discriminative features for classification. Removing the irrelevant features using ARD prevents the overfitting issue often seen in supervised learning<sup>78,81</sup>. Based on Table (2), the selected features include: 3 Fourier descriptors from complex, polar and farthest point angle signatures, as well as 2 entropies from the Gabor filters.

The textural features obtained from the proposed MBRBST method had a better classification performance than those obtained from the conventional ROI extraction and RBST methods. This indicates that the proposed amalgamation of morphological information in the textural features results in a more discriminative power. The consistent classification of the images obtained from three different sonography machines suggests that the performance of the proposed textural features can be independent from machine settings. An additional analysis to confirm this claim would involve a comparison of the results from each of the devices separately. This was, however, not possible at the time of writing this paper due to the small number of images. Moreover, it is noticeable that the proposed method is at an advantage to the other methods because this dataset was used in its development; even though cross-validation was used, this still biases performance in favor of the proposed method.

The proposed method is limited in using a fixed diameter for tumor boundary band extraction, impeding applications of MBRBST to tumors with a minimal size. A line of future work is to consider an adaptive method for tumor boundary extraction. Experimental results in Table (2) show that a combination of Fourier descriptors and their statistical features results in lower accuracies compared to using Fourier descriptors only. This is due to SLR's limited ability to select all relevant features when a large combination of features is being used. To alleviate this issue, incorporation of other classifiers alongside ARD can be considered. In addition, larger and more balanced datasets, and employing neural networks for feature extraction may increase the classification accuracy.

Three of the most frequently misclassified images were investigated and discussed with an expert radiologist. Accordingly, our false negatives have high malignancy risks and the false positive turned out to have low malignancy risks. To obviate these faults and to improve our algorithm, we propose combining imaging signs with the patient meta-data (i.e., age, ethnicity, genomics, smoking habits, etc.), which can be important for diagnosis. The proposed CAD systems is a complementary tool that can only aid the radiologists to conclude their diagnosis.

## VI. Conclusion

We proposed a CAD system for classification of benign and malignant tumors in 104 BUS images and compared the effectiveness of different features for classification. Tumors were delineated using a semi-supervised method to ensure a good quality in segmentation results. To classify each image, various forms of morphological and textural information were collected. From the segmented tumor 2D masks, 21 shape-based features were constructed. Next, 810 contour based features were generated from seven new and two existing tumor signatures (1D contour representations). A novel technique was proposed to unfold tumor boundary bands into images from which, by applying Gabor filters and computing entropies, 24 textural features were extracted (making a total of 855 features). We used a Bayesian extension of Logistic Regression with ARD mechanism for joint feature selection and classification. The selected features comprise of: 3 Fourier descriptors from complex, polar, and farthest point angle signatures, as well as 2 textural features. The proposed method achieved 97.12% accuracy, 93.75% sensitivity, and 98.61% specificity, outperforming the state-of-the-art methods applied on our images.

## Acknowledgments

The authors would like to thank Dr. Hamid Behnam<sup>27</sup> and Dr. Gomez Flores<sup>11,80</sup> for their support.

## Disclosure of Conflicts of Interest

The authors have no relevant conflicts of interest to disclose.

## References

1. Prabusankarlal KM, Thirumoorthy P, Manavalan R. Computer Aided Breast Cancer Diagnosis Techniques in Ultrasound: A Survey. *J Med Imaging Heal Informatics*. 2014;4(3):331-349. doi:10.1166/jmihi.2014.1269.
2. Cheng HD, Shan J, Ju W, Guo Y, Zhang L. Automated breast cancer detection and classification using ultrasound images: A survey. *Pattern Recognit*. 2010;43(1):299-317. doi:10.1016/j.patcog.2009.05.012.
3. Jalalian A, Mashohor SBT, Mahmud HR, Saripan MIB, Ramli ARB, Karasfi B. Computer-aided detection/diagnosis of breast cancer in mammography and ultrasound: A review. *Clin Imaging*. 2013;37(3):420-426. doi:10.1016/j.clinimag.2012.09.024.
4. Telagarapu P, Poonguzhali S. Analysis of Contourlet Texture Feature Extraction to Classify the Benign and Malignant Tumors from Breast Ultrasound Images. *Int J Eng Technol*. 2014;6(1):293-305.
5. Liu B, Cheng HD, Huang J, Tian J, Tang X, Liu J. Fully automatic and segmentation-robust classification of breast tumors based on local texture analysis of ultrasound images. *Pattern Recognit*. 2010;43(1):280-298. doi:10.1016/j.patcog.2009.06.002.
6. Su Y, Wang Y, Jiao J, Guo Y. Automatic detection and classification of breast tumors in ultrasonic images using texture and morphological features. *Open Med Inform J*. 2011;5(Suppl 1):26-37. doi:10.2174/1874431101105010026.
7. Liao YY, Tsui PH, Yeh CK. Classification of benign and malignant breast tumors by ultrasound B-scan and Nakagami-based images. *J Med Biol Eng*. 2010;30(5):307-312. doi:10.5405/jmbe.30.5.06.
8. El-Khateeb SM, Abou-Khalaf AE, Farid MM. A prospective study of three diagnostic sonographic methods in differentiation between benign and malignant salivary gland tumours. *Dentomaxillofacial Radiol*. 2014.
9. Gómez W, Leija L, Alvarenga A V., Infantosi AFC, Pereira WCA. Computerized lesion segmentation of breast ultrasound based on marker-controlled watershed transformation. *Med Phys*. 2010;37(1):82-95. doi:10.1118/1.3265959.
10. Gómez Flores W, Pereira WCDA, Infantosi AFC. Breast Ultrasound Despeckling Using Anisotropic Diffusion Guided by Texture Descriptors. *Ultrasound Med Biol*. 2014;40(11):2609-2621. doi:10.1016/j.ultrasmedbio.2014.06.005.
11. Gómez Flores W, Pereira WCDA, Infantosi AFC. Improving classification performance of breast lesions on ultrasonography. *Pattern Recognit*. 2015;48(4):1125-1136. doi:10.1016/j.patcog.2014.06.006.
12. Chang RF, Wu WJ, Moon WK, Chen DR. Automatic ultrasound segmentation and morphology based diagnosis of solid breast tumors. *Breast Cancer Res Treat*. 2005;89(2):179-185. doi:10.1007/s10549-004-2043-z.
13. Xian M, Zhang Y, Cheng HD. Fully automatic segmentation of breast ultrasound images based on breast characteristics in space and frequency domains. *Pattern Recognit*. 2015;48(2):485-497. doi:10.1016/j.patcog.2014.07.026.
14. Alvarenga AV, Infantosi a. FC, Pereira WC a, Azevedo CM. Assessing the performance of morphological parameters in distinguishing breast tumors on ultrasound images. *Med Eng Phys*. 2010;32(1):49-56. doi:10.1016/j.medengphy.2009.10.007.
15. Gómez W, Pereira WCA, Infantosi AFC, Díaz-Pérez A. Computerized diagnosis of breast lesions on ultrasonography. XXII Brazilian Congr Biomed Eng. 2010:399-402. <http://www.tamps.cinvestav.mx/~wgomez/documentos/CBEB2010.pdf>.
16. Chen C-M, Chou Y-H, Han K-C, et al. Breast lesions on sonograms: computer-aided diagnosis with nearly setting-independent features and artificial neural networks. *Radiology*. 2003;226(2):504-514. doi:10.1148/radiol.2262011843.
17. Sehgal CM, Cary TW, Kangas S a, et al. Computer-based margin analysis of breast sonography for differentiating malignant and benign masses. *J Ultrasound Med*. 2004;23(9):1201-1209. <http://www.ncbi.nlm.nih.gov/pubmed/15328435>.
18. Shanmuganathan S. Artificial Neural Network Modelling. *Stud Comput Intell*. 2016;628:1-14. doi:10.1007/978-3-319-28495-8.
19. Wu W, Lin S, Kyung W. Combining support vector machine with genetic algorithm to classify ultrasound breast tumor images. *Comput Med Imaging Graph*. 2012;36:627-633.
20. Shen WC, Chang RF, Moon WK, Chou YH, Huang CS. Breast Ultrasound Computer-Aided Diagnosis Using BI-RADS Features. *Acad Radiol*. 2007;14(8):928-939. doi:10.1016/j.acra.2007.04.016.
21. Kohavi R, George H. Wrappers for feature subset selection. *Artif Intell*. 1997;97(1-2):273-324. doi:10.1016/S0004-3702(97)00043-X.
22. Abdelwahed NMA, Eltoukhy MM, Wahed ME. Computer Aided System for Breast Cancer Diagnosis in Ultrasound Images. *J Ecol Heal Environ*. 2015;76(3):71-76.
23. Lokesh B, Shailaja K, Nanda S. Segmentation And Classification Of Breast Lesions In Ultrasound Images. *Int J Sci Technol ogy Res*. 2014;3(6):238-242.
24. Moon WK, Lo C, Chang JM. Quantitative Ultrasound Analysis for Classification of BI-RADS Category 3 Breast Masses. 2013:1091-1098. doi:10.1007/s10278-013-9593-8.
25. Alvarenga AVAV, Infantosi AFC, Pereira WC a, Azevedo CM. Assessing the combined performance of texture and morphological parameters in distinguishing breast tumors in ultrasound images. *Med Phys*. 2012;39(12):7350-7358. doi:10.1118/1.4766268.
26. Zakeri FS, Behnam H, Ahmadinejad N. Classification of benign and malignant breast masses based on shape and texture features in sonography images. *J Med Syst*. 2012;36(3):1621-1627. doi:10.1007/s10916-010-9624-7.
27. Behnam H, Zakeri FS, Ahmadinejad N. Breast mass classification on sonographic images on the basis of shape analysis. *J Med Ultrason*. 2010;37(4):181-186. doi:10.1007/s10396-010-0278-3.
28. Alvarenga AVAV, Infantosi AFC, Pereira WC a, Azevedo CM. Assessing the performance of morphological parameters in distinguishing breast tumors on ultrasound images. *Med Eng Phys*. 2010;32(1):49-56. doi:10.1016/j.medengphy.2009.10.007.
29. Wu WJ, Moon WK. Ultrasound Breast Tumor Image Computer-Aided Diagnosis With Texture and Morphological Features. *Acad Radiol*. 2008;15(7):873-880. doi:10.1016/j.acra.2008.01.010.
30. Horsch K, Ceballos AF, Giger ML, et al. Optimizing feature selection across a multimodality database in computerized classification of breast lesions. In: *Medical Imaging 2002. International Society for Optics and Photonics*; 2002:986-992.
31. Kim KG, Kim JH, Min BG. Classification of malignant and benign tumors using boundary characteristics in breast ultrasonograms. *J Digit*

- Imaging. 2002;15 Suppl 1(March):224-227. doi:10.1007/s10278-002-5038-5.
32. Song JH, Venkatesh SS, Conant E a., Arger PH, Sehgal CM. Comparative analysis of logistic regression and artificial neural network for computer-aided diagnosis of breast masses. *Acad Radiol.* 2005;12(4):487-495. doi:10.1016/j.acra.2004.12.016.
  33. Huang Y-L, Wang K-L, Chen D-R. Diagnosis of breast tumors with ultrasonic texture analysis using support vector machines. *Neural Comput Appl.* 2006;15(2):164-169. doi:10.1007/s00521-005-0019-5.
  34. Lo C-M, Moon WK, Huang C-S, Chen J-H, Yang M-C, Chang R-F. Intensity-Invariant Texture Analysis for Classification of BI-RADS Category 3 Breast Masses. *Ultrasound Med Biol.* 2015;41(7):2039-2048. doi:10.1016/j.ultrasmedbio.2015.03.003.
  35. Yang MC, Moon WK, Wang YCF, et al. Robust texture analysis using multi-resolution gray-scale invariant features for breast sonographic tumor diagnosis. *IEEE Trans Med Imaging.* 2013;32(12):2262-2273. doi:10.1109/TMI.2013.2279938.
  36. Yap MH, Edirisinghe EA, Bez HE. A Comparative Study in Ultrasound Breast Imaging Classification. *SPIE Med Imaging Int Soc Opt Photonics.* 2009;7259:72591S-11. doi:10.1117/12.811208.
  37. Abdel-Zaher AM, Eldeib AM. Breast cancer classification using deep belief networks. *Expert Syst Appl.* 2016;46(November):139-144. doi:10.1016/j.eswa.2015.10.015.
  38. Jadoon MM, Zhang Q, Haq IU, Butt S. Three-class mammogram classification based on descriptive CNN features. *Biomed Res Int.* 2017.
  39. Shelgaonkar SL, Nandgaonkar AB, Liu Z, et al. Deep Belief Network for the Enhancement of Ultrasound Images with Pelvic Lesions. *J Intell Syst.* 2017;0(0):447-455. doi:10.1515/jisys-2016-0112.
  40. MacKay DJC. Bayesian Interpolation. *Neural Comput.* 1992;4(3):415-447. doi:10.1162/neco.1992.4.3.415.
  41. Ueno E, Shiina T, Kubota M. Research and Development in Breast Ultrasound. Springer Science & Business Media; 2006. doi:10.1007/b138439.
  42. Heckbert PS. *Graphic Gems IV.* 1994:474-485.
  43. Pavlidis T. *Algorithms for Graphics and Image Processing.* Springer Science & Business Media; 2012.
  44. Software G. *Didger 5 Full User's Guide - Golden Software.* 2013.
  45. U.Fischer, F.Baum, S.Luftner-Nagel. *Breast Imaging.* Vol 53.; 2008.
  46. Kasaudhan R, Heo TK, Jeon SI, Son SH. Similarity measurement with combination of mesh distance fourier transform and global features in 2D binary image. In: *Proceedings of the 2015 Conference on Research in Adaptive and Convergent Systems.* ; 2016:2176-2181. doi:10.1145/2851613.2851991.
  47. Kauppinen H, Seppanen T, Pietikainen M. An experimental comparison of autoregressive and Fourier-based descriptors in 2D shape classification. *IEEE Trans Pattern Anal Mach Intell.* 1995;17(2):201-207. doi:10.1109/34.368168.
  48. Mattrand C, Béakou A, Charlet K. Numerical modeling of the flax fiber morphology variability. *Compos Part A Appl Sci Manuf.* 2014;63:10-20. doi:10.1016/j.compositesa.2014.03.020.
  49. Shu X, Pan L, Wu XJ. Multi-scale contour flexibility shape signature for Fourier descriptor. *J Vis Commun Image Represent.* 2015;26:161-167. doi:DOI 10.1016/j.jvcir.2014.11.007.
  50. Varga D. American Hand Sign Recognition in Video Streams. 2014:162-166. [http://eprints.sztaki.hu/8221/1/Varga\\_162\\_2698331\\_ny.pdf](http://eprints.sztaki.hu/8221/1/Varga_162_2698331_ny.pdf).
  51. Yang M, Kpalma K, Ronsin J. A survey of shape feature extraction techniques. In: *Pattern Recognition.* ; 2008:43-90. doi:10.5772/6237.
  52. Zhang D, Lu G. Study and evaluation of different Fourier methods for image retrieval. *Image Vis Comput.* 2005;23(1):33-49. doi:10.1016/j.imavis.2004.09.001.
  53. El-ghazal A, Basir O, Belkasim S. Farthest point distance: A new shape signature for Fourier descriptors. *Signal Process Image Commun.* 2009;24(7):572-586. doi:10.1016/j.image.2009.04.001.
  54. Mani MR, Varma GPS, D.M. P, Satyanarayana C. Design of a Novel Shape Signature by Farthest Point Angle for Object Recognition. *Int J Image, Graph Signal Process.* 2014;7(1):35-46. doi:10.5815/ijigsp.2015.01.05.
  55. Diao X, Wang T, Yang Y, Chen S. Computer-aided Diagnosis of Breast Tumor Based on B-mode Ultrasound and Color Doppler Flow Imaging. *Biomed Eng Informatics.* 2009.
  56. Joo S, Yang YS, Moon WK, Kim HC. Computer-aided diagnosis of solid breast nodules: Use of an artificial neural network based on multiple sonographic features. *IEEE Trans Med Imaging.* 2004;23(10):1292-1300. doi:10.1109/TMI.2004.834617.
  57. Diao X, Zhang X, Wang T, Chen S-P, Yang Y, Zhong L. Highly sensitive computer aided diagnosis system for breast tumor based on color Doppler flow images. *J Med Syst.* 2011;35(5):801-809. doi:10.1007/s10916-010-9461-8.
  58. Loncaric S. A survey of shape analysis techniques. *Pattern Recognit.* 1998;31(8):983-1001. doi:10.1016/S0031-2023(97)00122-2.
  59. Zahn CT, Roskies RZ. Fourier Descriptors for Plane Closed Curves. *IEEE Trans Comput.* 1972;C-21(3):269-281.
  60. Jalba AC, Wilkinson MHF, Roerdink JBTM. Shape Representation and Recognition Through Morphological Curvature Scale Spaces. *IEEE Trans Image Process.* 2006;15(2):331-341.
  61. Silva PD, Bhuvanewari P. Various Shape Descriptors in Image Processing – A Review. 2015;4(3):2338-2342.
  62. González RC, Woods RE. *Digital Image Processing Using MATLAB.* Upper Sadd. New Jersey: "I." Upper Saddle River, New Jersey (2004).; 2004. <http://books.google.co.uk/books?id=738oAQAAMAAJ>.
  63. Alto H, Rangayyan RM, Leo Desautels JE. Content-based retrieval and analysis of mammographic masses. *J Electron Imaging.* 2007;16(1):023016-023016. doi:10.1117/1.1902996.
  64. Rangayyan RM, El-Faramawy NM, Desautels JE, Alim O a. Measures of acutance and shape for classification of breast tumors. *IEEE Trans Med Imaging.* 1997;16(6):799-810. doi:10.1109/42.650876.
  65. Rangayyan RM, Elkadiki SG. Algorithm for the computation of region-based image edge profile acutance. *J Electron Imaging.* 1995;4(1):62-70. <http://link.aip.org/link/?JEL/4/62/1>.

66. Rangayyan RM, Ayres FJ, Leo Desautels JE. A review of computer-aided diagnosis of breast cancer: Toward the detection of subtle signs. *J Franklin Inst.* 2007;344(3-4):312-348. doi:10.1016/j.jfranklin.2006.09.003.
67. Sehgal CM, Weinstein SP, Arger PH, Conant EF. A Review of Breast Ultrasound. *J Mammary Gland Biol Neoplasia.* 2006;11(2):113-123. doi:10.1007/s10911-006-9018-0.
68. Sahiner B, Chan H-P, Petrick N, Goodsitt MM, Helvie MA. Characterization of masses on mammograms: Significance of using the rubber-band straightening transform. In: *Proceedings of SPIE - The International Society for Optical Engineering.* Vol 3034. ; 1997:491-500. doi:10.1117/12.274135.
69. Sahiner B, Chan HP, Petrick N, Helvie MA, Goodsitt MM. Computerized characterization of masses on mammograms: the rubber band straightening transform and texture analysis. *Med Phys.* 1998;25(4):516-526. doi:10.1118/1.598228.
70. Sahiner B, Chan H, Petrick N, Helvie MA, Adler DD, Goodsitt MM. Classification of masses on mammograms using rubber-band straightening transform and feature analysis. *Int Soc Opt Photonics.* 2710. doi:10.1117/12.237963.
71. Buciu I, Gacsadi A. Gabor wavelet based features for medical image analysis and classification. *2009 2nd Int Symp Appl Sci Biomed Commun Technol.* 2009:1-4. doi:10.1109/ISABEL.2009.5373659.
72. Buciu I, Gacsadi A. Directional features for automatic tumor classification of mammogram images. *Biomed Signal Process Control.* 2011;6(4):370-378. doi:10.1016/j.bspc.2010.10.003.
73. Ergin S, Kilinc O. A new feature extraction framework based on wavelets for breast cancer diagnosis. *Comput Biol Med.* 2014;51:171-182. doi:10.1016/j.combiomed.2014.05.008.
74. Ferrari RJ, Rangayyan RM, Desautels JEL, Frère a. F. Analysis of asymmetry in mammograms via directional filtering with Gabor wavelets. *IEEE Trans Med Imaging.* 2001;20(9):953-964. doi:10.1109/42.952732.
75. Salve MSM. Classification of Mammographic images using Gabor Wavelet and Discrete Wavelet Transform. *Int J Adv Res Electron Commun Eng.* 2013;2(5):573-578.
76. Mirzapour F, Ghassemian H. Using GLCM and Gabor Filters for Classification of PAN Images. In: *Electrical Engineering (ICEE), 2013 21st Iranian Conference on IEEE.* ; 2013. doi:10.1109/IranianCEE.2013.6599565.
77. Gómez W, Pereira WCA, Infantosi AFC. Intensity-Invariant Texture Features for Breast Ultrasound Classification. 2014;(1):529-532.
78. Yamashita O. Sparse estimation automatically selects voxels relevant for the decoding of fMRI activity patterns. *Neuroimage.* 2008;42(4):1414-1429. doi:10.1016/j.neuroimage.2008.05.050.Sparse.
79. Socialium R, Oeconomicarumque. *Theory and Implementation of Anticipatory Data Mining.*; 2006.
80. Rodríguez-Cristerna Arturo, Gómez-Flores Wilfrido and A-PWC de. BUSAT : A MATLAB Toolbox for Breast Ultrasound Image Analysis. 2017;1:268-277. doi:10.1007/978-3-319-59226-8.
81. Bishop CM. *Pattern Recognition and Machine Learning.* Machine Learning; 2006.

## VII. Appendices

### Appendix A: Morphological Shape Based Features

Table (6): The definition of implemented Morphological-Shape-Based Features used for breast tumor diagnosis.

Feature name	Definition	Description	References
Form-factor	$\frac{4\pi \cdot \text{Area}}{\text{Perimeter}}$	Area and Perimeter are the area and perimeter of the tumor.	11,12
Compactness (Circularity)	$\frac{\text{Perimeter}^2}{\text{Area}}$		14,2,31,55
Aspect-ratio	$\frac{\text{Max\_diameter}}{\text{Min\_diameter}}$	Max_diameter and Min_diameter are the maximal and minimal diameters of a tumor at different projection angles.	11,12,2,36
Roundness	$\frac{4 \cdot \text{Area}}{\pi \cdot \text{Max\_diameter}^2}$		11,12,36
Long axis to short axis ratio (L: S)	$\frac{\text{Major\_axis}}{\text{Minor\_axis}}$	Major_axis and Minor_axis are the major (long) axis and minor (short) axis of the equivalent ellipse that has the same normalized second central moments as the tumor.	2,36,16
Convexity	$\frac{\text{Convex\_perimeter}}{\text{Perimeter}}$	Convex_perimeter and Convex_area are the perimeter and the area of the convex hull of a tumor (See Fig. A1b).	11,12,36,15,51
Solidity (Overlap-ratio)	$\frac{\text{Area}}{\text{Convex\_area}}$		11,12,14,36,15,51,26
Difference area	Convex_area - Area		27
Normalized Residual Value (NRV)	$\frac{\text{Convex\_area} - \text{Area}}{\text{Convex\_perimeter}}$		11,14
Elongation	$\frac{\text{Length\_bounding\_rectangle}}{\text{Width\_bounding\_rectangle}}$		Length_bounding_rectangle, Width_bounding_rectangle and Area_bounding_rectangle are the length, width and area of the minimal rectangle that including the tumor, respectively.
Extent	$\frac{\text{Area}}{\text{Area\_bounding\_rectangle}}$	11,12,36,51	
Morphological-closing ratio (Mshape)	$\frac{\text{Area}}{\text{Morphological\_closing\_area}}$	Morphological_closing_area is shown in Fig. A1c	14
Orientation	The angle between the x-axis and the major axis of the ellipse with the same second-moments as the tumor.		11,20
Eccentricity	The ratio of the distance between the foci of the ellipse with the same second moment as the tumor, to its major axis length.		26
Elliptic-normalized skeleton	the number of skeleton points normalized by the circumference of the equivalent ellipse of the lesion.	Let R and B <sub>R</sub> denote a region and the set of its boundary points. The skeleton of R, is a set of points X where for each point x ∈ X, there exist at least two boundary points, p <sub>i</sub> and p <sub>j</sub> , in B <sub>R</sub> so d(x, p <sub>i</sub> ) = d(x, p <sub>j</sub> ) = min{d(x, p <sub>k</sub> )   p <sub>k</sub> ∈ B <sub>R</sub> }, where d(.) can be any preferred distance metric (See Fig. A1d).	11,2,16
Number of skeleton end-points			11
Mean-variation	mean value of variation function	Variation function is the projection of the distance between the farthest pixels of a tumor region at all angles.	27
Variance-variation	variance value of variation function		
Skewness-variation	skewness value of variation function		
Kurtosis-variation	kurtosis value of variation function		
Entropy-variation	entropy value of variation function		

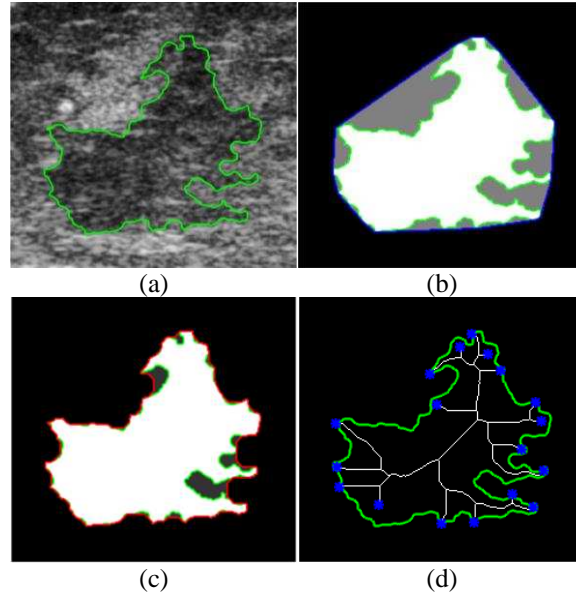


Fig. A1. A BUS image of a malignant tumor and its contour (green color) (a), difference of area (in grey) between the convex hull area and the tumor area (b), difference of area (in dark grey) between the morphological closing area and the tumor area (c), and the skeleton of the tumor (white) and the skeleton end-points (blue stars) (d), see Table 6.

## Appendix B: Signatures of tumor contour

Shape signatures can be real or complex<sup>51-53,47</sup>. In the following, the signatures implemented in this paper are explained. The coordinates of contour points are denoted by  $(x(t), y(t))$ ,  $t = 1, 2, \dots, N$ , in which  $N$  is the number of these points, and coordinates of tumor center are denoted by  $(x_c, y_c)$ .

### 1. Complex Coordinates (Z)

Complex coordinates function is a complex representation of the coordinates of boundary points in Eq. 1. Shifted coordinates functions is used to remove bias effects<sup>51-53,47,46,48-50</sup>.

$$Z(t) = (x(t)-x_c) + j(y(t)-y_c) \quad (1)$$

### 2. Radial distance (R)

The value of this signature as expressed in Eq. 2, is obtained as the distance between the contour points and the tumor center (Fig. A2a)<sup>51-53,47,46,48,50,54</sup>.

$$R(t) = \sqrt{(x(t)-x_c)^2 + (y(t)-y_c)^2} \quad (2)$$

### 3. Polar coordinates (PC)

The combination of the radial distance  $R(t)$  and the polar angle  $\theta(t)$  defines the polar coordinates signature as expressed in Eq. 3 (Fig. A2b)<sup>53</sup>.

$$PC(t) = R(t) + j\theta(t) \quad (3)$$

### 4. Farthest point distance (FPD)

For a point  $(x(t), y(t))$ , FPD is the sum of radial distance of this point and that of the farthest point to it on the contour, denoted by  $(x_{fp}(t), y_{fp}(t))$  (Eq. 4, Fig. A2c)<sup>53,49,54</sup>.

$$FPD(t) = \sqrt{(x(t)-x_c)^2 + (y(t)-y_c)^2} + \sqrt{(x_{fp}(t)-x_c)^2 + (y_{fp}(t)-y_c)^2} \quad (4)$$

### 5. Farthest Point Angle (FPA)

According to Eq. 5 the angle between the radial distance of a contour point ( $m_1$ ) and the radial distance of the corresponding farthest point ( $m_2$ ) results in the value of this function (Fig. A2d)<sup>54</sup>.

$$\text{FPA}(t) = \text{Tan}^{-1} \left( \frac{m_2 - m_1}{1 + m_1 \times m_2} \right) \quad (5)$$

#### 6. Angular function ( $\varphi$ )

The angular function  $\varphi(t)$  demonstrates the changes of angular contour directions. This signature, shown in Eq. 6, is obtained by the tangent angle for a window  $w$ . However, since the values of tangent angle are assumed to lie in a range of length,  $\varphi(t)$  contains discontinuities with  $2\pi$  size. Fig. A2e shows the tangent angle of a contour point for a window size  $w = 5$ <sup>51-53,59</sup>.

$$\varphi(t) = \text{Tan}^{-1} \left( \frac{y(t) - y(t-w)}{x(t) - x(t-w)} \right) \quad (6)$$

#### 7. Angular radial coordinates (ARC)

This signature, expressed in Eq. 7, is the combination of the radial distance  $R(t)$  and the angular function  $\varphi(t)$  (similar to the polar coordinates signature)<sup>53</sup>.

$$\text{ARC}(t) = R(t) + j\varphi(t) \quad (7)$$

#### 8. Contour curvature (K)

Contour curvature is defined as the differentiation of successive tangent angles calculated in a window  $w$ , expressed in Eq. 8. Fig. A2f shows the successive contour angles calculated in a window of size  $w = 5$ <sup>52,47,49,54,59-61</sup>.

$$K(t) = \varphi(t) - \varphi(t-1) \quad (8)$$

#### 9. Triangle area function (TAF)

The value of this function is obtained according to the area of the triangle made by two successive contour points and the tumor center in Fig. A2g<sup>51-53,49</sup>.

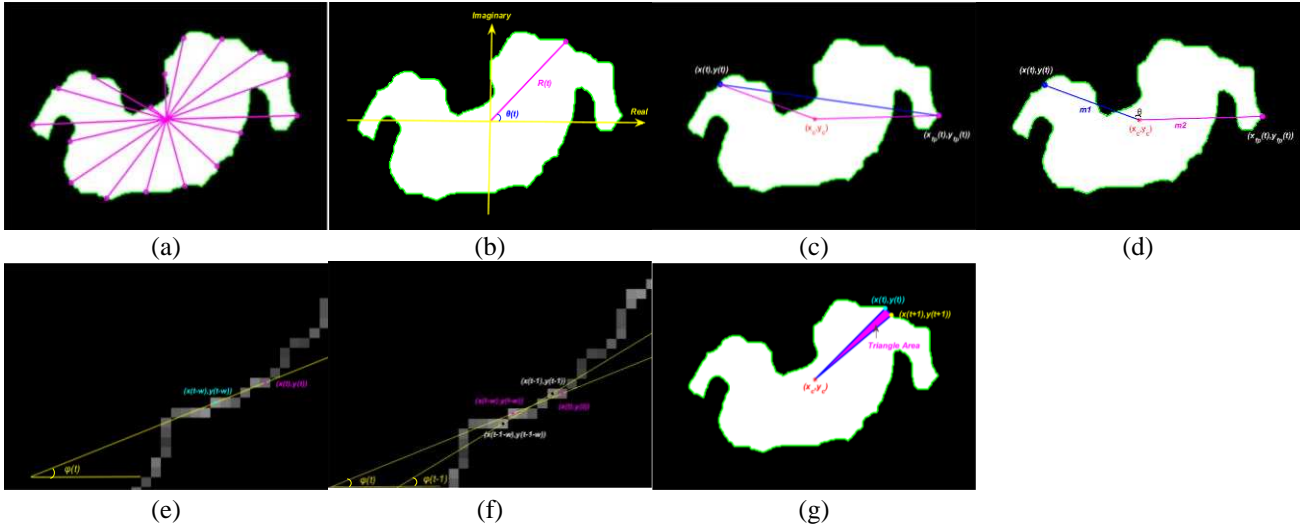


Fig. A2. (a) The contour of the tumor (in green), the center of the tumor (\*), and several representative radial distances (Magenta lines) that are equal to the distance between the contour points and the tumor center. (b) A display of the polar coordinates system at a contour point, the radial distance  $R(t)$  (Magenta line) and polar angle  $\theta(t)$ . (c) The point  $(x(t), y(t))$  and the corresponding farthest point  $(x_{fp}(t), y_{fp}(t))$ , adding the radial distances of these points (magenta lines) indicates FPD for given point  $(x(t), y(t))$ . (d) The angle between the radial distance of the point  $(x(t), y(t))$  ( $m_1$ ) (blue color) and the radial distance of the corresponding farthest point  $(x_{fp}(t), y_{fp}(t))$  ( $m_2$ ) (magenta color) gives us FPA signature for point  $(x(t), y(t))$ . (e) The angular function is calculated for a window size  $w = 5$ . (f) Two successive tangent angles  $\varphi(t)$  and  $\varphi(t-1)$  that are calculated for a window with  $w = 5$ . Contour curvature is defined as  $\varphi(t) - \varphi(t-1)$ . (g) The contour of tumor (in green) and the area of the triangle formed by the tumor center (\*) and two successive contour points (points on the contour are in cyan and yellow).

### Appendix C: Fourier descriptors; invariance to translation, rotation and scale

For a sample signature  $s(t)$ ,  $t = 0, 1, \dots, L-1$  after an  $L$ -point normalization, the Fourier descriptors are given in

Eq. 9<sup>51,47,46,50,54</sup>.

$$FD_n = \frac{1}{L} \sum_{t=0}^{L-1} s(t) \exp\left(\frac{-j2\pi t n}{L}\right), n = 0, 1, \dots, L-1 \quad (9)$$

### 1. Translation invariance

The FDs are translation invariant, because all the nine explained signatures are invariant under translation <sup>51,47,46</sup>.

### 2. Rotation invariance

Since phase information is ignored in our application, and only the magnitude values of the FDs are used, FDs are rotation invariant <sup>47,46</sup>.

### 3. Scale invariance

For complex signatures such as complex coordinates, polar coordinates, and angular radial coordinates, all the L descriptors except the first one (DC component) are necessary to index the shape. Scale normalization is achieved by dividing the magnitude values of all the other descriptors by the magnitude value of the second descriptor (Eq. 10). <sup>53,47,50</sup>

$$f = \left[ \frac{|FD_2|}{|FD_1|}, \frac{|FD_3|}{|FD_1|}, \dots, \frac{|FD_{L-1}|}{|FD_1|} \right] \quad (10)$$

Since the functions of centroid distance, farthest point distance, farthest point angle, angular function, contour curvature, and triangle area signatures are real, only L/2 frequencies in the Fourier transform are different, therefore just half of the FDs are used. Scale invariance, according to Eq. 11 is obtained by dividing the magnitude values of the first half of FDs by the DC component. <sup>53,47,49</sup>

$$f = \left[ \frac{|FD_2|}{|FD_0|}, \frac{|FD_3|}{|FD_0|}, \dots, \frac{|FD_{L/2}|}{|FD_0|} \right] \quad (11)$$

## Appendix D: Gabor filter formulation

The direction feature of Gabor wavelet makes it appropriate for several applications, including image texture analysis and image retrieval. Gabor filters used in image processing are two-dimensional and have specific scales and directions. A complex Gabor wavelet is obtained as the production of a Gaussian kernel with a complex sinusoid <sup>72</sup>.

Assuming the mother wavelet  $\varphi(x,y)$  given in Eq. 12, the set of wavelets are made by Eq. 13 in which  $h_{s,d}(x,y)$  is the impulse response of Gabor filter in scale  $s$  and direction  $d$ . Also,  $x$  and  $y$  are the row and column of the impulse response, and  $\sigma_x$  and  $\sigma_y$  are their standard deviations, respectively. The entire image is the filter bank input. Definitions of  $X$  and  $Y$  are given in Eq. 14 and 15, respectively.

$$\varphi(x,y) = \frac{1}{2\pi\sigma_x\sigma_y} \exp\left\{-\frac{1}{2}\left(\frac{x^2}{\sigma_x^2} + \frac{y^2}{\sigma_y^2}\right) + 2\pi j U_h x\right\} \quad (12)$$

$$h_{s,d}(x,y) = \left(\frac{U_h}{U_l}\right)^{\frac{-s}{s-1}} \cdot \varphi(X,Y) \quad (13)$$

$$X = \left(\frac{U_h}{U_l}\right)^{\frac{-s}{s-1}} \left[ (x-x_0) \cos\left(\frac{d\pi}{N_d}\right) + (y-y_0) \sin\left(\frac{d\pi}{N_d}\right) \right] \quad (14)$$

$$Y = \left(\frac{U_h}{U_l}\right)^{\frac{-s}{s-1}} \left[ -(x-x_0) \sin\left(\frac{d\pi}{N_d}\right) + (y-y_0) \cos\left(\frac{d\pi}{N_d}\right) \right] \quad (15)$$

The filter's output is complex; therefore, magnitudes of these values are used. In the overhead equations,  $s = 1, \dots, N_s$  and  $d = 1, \dots, N_d$  are the scale and direction of wavelet parameters,  $(x_0, y_0)$  is the filter origin in space, and  $U_l$  and  $U_h$  are the minimum and the maximum central frequencies of the filters, respectively <sup>76</sup>.

In this study, we set  $N_s = 6$ ,  $N_d = 4$ ,  $U_h = 0.49$ , and  $U_l = 0.01$ .

## Appendix E: Sparse logistic regression

Logistic regression, used for solving binary classification, is a probabilistic model, parameters of which are estimated using the Maximum Likelihood Method. The weighted feature values represents the linear discriminant function in Eq. 16 that splits two classes, namely  $S_1$  and  $S_2$ .

$$f(x; w) = \sum_{i=1}^D w_d x_d + w_0 \quad (16)$$

In Eq. 16,  $\mathbf{x} = (x_1, \dots, x_D)^t \in \mathbb{R}^D$  is the input feature vector in D-dimensional space and  $\mathbf{w} = (w_0, w_1, \dots, w_D)^t$  is the weight vector including a bias term, where we set  $w_0 = 0$ . Using a logistic sigmoid function (Eq. 17), LR calculates the probability that  $x$  belongs to classes  $S_1$  and  $S_2$  (Eq. 18).

$$\sigma(x) = \frac{1}{1 + \exp(-x)} \quad (17)$$

$$p \triangleq P(S_2|x) = \sigma(w^t x) \Rightarrow P(S_1|x) = 1-p \quad (18)$$

We define a binary random variable  $y$  that is 0 for  $x \in S_1$  and 1 for  $x \in S_2$ . Having  $N$  iid<sup>1</sup> input–output data samples  $\{(x_1, y_1), \dots, (x_N, y_N)\}$ , the likelihood function is given as Eq. 19.

$$P(y|X, w) = P(y_1, \dots, y_N | x_1, \dots, x_N, w) = \prod_{n=1}^N P(y_n | x_n, w) = \prod_{n=1}^N p_n^{y_n} (1-p_n)^{1-y_n} \quad (19)$$

where  $p_n = P(y_n = 1 | x_n, w) = \sigma(w^t x_n)$ . Therefore, the log-likelihood function becomes as Eq. 20.

$$l(w) = \sum_{i=1}^N [y_n \log p_n + (1-y_n) \log(1-p_n)] \quad (20)$$

The optimal value of  $w$  is achieved by maximizing  $l(w)$ . It can be proven that since the Hessian of this function is positive definite for all  $w$ , a unique global maximum always exists. In this classifier, the contour between two classes is determined by the hyper-plane  $f(x; w) = 0$ . So, a test sample  $x_{\text{test}}$  is assigned to class  $S_2$ , if  $f(x_{\text{test}}; w) > 0$ , and assigned to class  $S_1$ , if  $f(x_{\text{test}}; w) < 0$ .

Automatic Relevance Detection (ARD) is an efficient algorithm for eliminating irrelevant features. It moves the weights corresponding to less relevant features towards zero; making the weight vector sparse. ARD uses a Gaussian prior with a zero mean and a diagonal covariance matrix (the diagonal elements are tunable hyper-parameters) to define the possible range of weight parameters.

Sparse Logistic Regression (SLR) is made by combining LR and ARD. SLR, a Bayesian extension of LR, performs feature selection and training of the model parameters for classification, simultaneously. It employs ARD to determine the relevance of each feature by estimating its corresponding weight. This procedure involves three tasks: feature selection, training of the classifier, and evaluation of generalization performance. With ARD algorithm, SLR assumes a prior for weight vector as expressed in Eq. 21.

$$P(w_d | \alpha_d) = N(0, \alpha_d^{-1}), \quad d = 1, \dots, D \quad (21)$$

where  $w_d$  is the  $d^{\text{th}}$  element in  $\mathbf{w}$  and  $\alpha_d$  is its corresponding relevance parameter. The prior distribution for each  $w_d$  is assumed to be a normal distribution with a zero mean. Also, the prior distribution for  $\alpha_d$ 's is given in Eq. 22.

$$P_o(\alpha_d) = \alpha_d^{-1}, \quad d = 1, \dots, D \quad (22)$$

The hyper-parameter  $\alpha_d$ , the relevance parameter, controls the possible range of its corresponding weight parameter,  $w_d$ . A small relevance parameter results in a broadly distributed probability, leading to large values for the weight parameter (Fig. A3a). When the relevance parameter is large, the probability distribution of the prior knowledge has a high peak at zero. This biases the estimated parameter towards zero (Fig. A3b).

Using ARD<sup>78</sup>, an iterative algorithm estimates relevance parameters and the posterior distributions of the model. The estimated relevance parameters for irrelevant features diverge to infinity resulting their corresponding weight parameters to converge to zero. This way, the irrelevant features are eliminated and not used in classification.

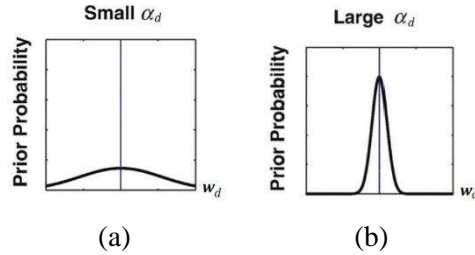


Fig. A3. Small values of the relevance parameter result in broad probability distributions and large values of estimated weight parameter (a) and large values of the relevance parameter result in narrow probability distributions and zero values of estimated weight parameter (b)<sup>78</sup>.

<sup>1</sup> independent and identically distributed

Appendix F: Categories of used features

Table (7): The explanation of features used based on their numbers.

Feature ID	Feature Name	Feature category	
F1	Form-factor	Shape-Based Features (F1-F21)	Morphological Features (F1-F831)
F2	Aspect-ratio		
F3	Long axis to short axis ratio		
F4	Roundness		
F5	Convexity		
F6	Extent		
F7	Solidity		
F8	Orientation		
F9	Eccentricity		
F10	Elongation		
F11	Difference area		
F12	Normalized Residual Value		
F13	Circularity		
F14	Mshape		
F15	Mean_Variation		
F16	Variance_Variation		
F17	Skewness_Variation		
F18	Kurtosis_Variation		
F19	Entropy_Variation		
F20	Elliptic-normalized skeleton		
F21	Number of skeleton end-points		
F22-F27	Mean, Standard deviation, Roughness index, Smoothness index, Zero crossing, and Area ratio of 'R' signature	Spatial information (F22-F42)	Morphological Features (F1-F831)
F28-F32	Mean, Standard deviation, Roughness index, Smoothness index, and Zero crossing of 'FPD' signature		
F33-F37	Mean, Standard deviation, Roughness index, Smoothness index, and Zero crossing of 'FPA' signature		
F38-F42	Mean, Standard deviation, Roughness index, Smoothness index, and Zero crossing of 'TAF' signature		
F43-F168	Fourier descriptors of 'Z' signature	Fourier descriptors (F43-F804)	Morphological Features (F1-F831)
F169-F294	Fourier descriptors of 'PC' signature		
F295-F358	Fourier descriptors of 'R' signature		
F359-F422	Fourier descriptors of 'FPD' signature		
F423-F486	Fourier descriptors of 'FPA' signature		
F487-F550	Fourier descriptors of ' $\phi$ ' signature		
F551-F676	Fourier descriptors of 'ARC' signature		
F677-F740	Fourier descriptors of 'K' signature		
F741-F804	Fourier descriptors of 'TAF' signature		
F805-F807	Mean, Variance, and Entropy of 'Z' signature		
F808-F810	Mean, Variance, and Entropy of 'PC' signature		
F811-F813	Mean, Variance, and Entropy of 'R' signature		
F814-F816	Mean, Variance, and Entropy of 'FPD' signature		
F817-F819	Mean, Variance, and Entropy of 'FPA' signature		
F820-F822	Mean, Variance, and Entropy of ' $\phi$ ' signature		
F823-F825	Mean, Variance, and Entropy of 'ARC' signature		
F826-F828	Mean, Variance, and Entropy of 'K' signature		
F829-F831	Mean, Variance, and Entropy of 'TAF' signature		
F832-F855	the entropy of filtered MBRBST images	statistical features of Fourier descriptors	Contour-Based (F22-F831)
		Textural Features	